Geophys. J. Int. (1996) **124,** 323–340

TREITEL SECTION

Two-dimensional velocity models from wide-angle seismic data by wavefield inversion

R. G. Pratt, Z.-M. Song, P. Williamson and M. Warner
Department of Geology, Imperial College, London SW7 2BP, *UK*

Accepted 1994 September 14. Received 1994 September 8; in original form 1994 June 1

SUMMARY

Modern wide-angle surveys are often multi-fold and multi-channel, with densely sampled source and receiver spacings. Such closely spaced data are potentially amenable to multi-channel techniques involving wavefield propagation methods, such as those commonly used in reflection data processing. However, the wide-angle configuration requires techniques capable of handling very general wave types, including those not commonly used in reflection seismology. This is a situation analogous to that faced in cross-borehole seismics, where similar wave types are also recorded. In a real cross-borehole example, we compare pre-stack migration, traveltime tomography and wavefield inversion. We find that wavefield inversion produces images that are quantitative in velocity (as are the tomograms) but are of significantly higher resolution; the wavefield inversion results have a resolution comparable to that of the (qualitative) pre-stack migration images. We seek to extend this novel development to the larger-scale problem of crustal imaging.

An essential element of the approach we adopt is its formulation entirely within the temporal frequency domain. This has three principal advantages: (1) we can choose to 'decimate' the data, by selecting only a limited number of frequency components to invert, thus making inversion of data from large numbers of source positions feasible; (2) we can mitigate the notorious non-linearity of the seismic inverse problem by progressing from low-frequency components in the data to high-frequency components; and (3) we can include in the model any arbitrary frequency dependence of inelastic attenuation factors, $Q(\omega)$, and indeed solve for the spatial distribution of Q.

An initial synthetic test with an anomaly located within the middle crust yields a velocity image with the correct structural features of the anomaly and the correct magnitude of velocity anomaly. This is related to the fact that the reconstruction is obtained from forward-scattered waves. Under these conditions, the method thus behaves much like tomography. A second test with a deeper, more extensive anomaly yields an image with the correct velocity polarity and the correct location, but with a deficiency in low and high wavenumbers. In this case, this is because the reconstruction is obtained from backscattered waves; under these conditions the method behaves not like tomography, but like migration.

A more extensive test, based on a large wide-angle survey in south-eastern California and western Arizona, demonstrates a real potential for high-resolution imaging of crustal structures. Although our results are limited by the acoustic approximation and by the relatively low frequencies that we can model today, the images are sufficiently encouraging to warrant future research. The problem of local minima in the objective function is the most significant practical problem with our method, but we propose that appropriate 'layer' stripping methods can handle this problem.

Key words: crustal structure, finite-difference methods, refraction seismology, seismic tomography.

INTRODUCTION

Conventional surface-seismic reflection geometries are optimally designed to image sub-horizontal structure in a stratified earth. With this geometry, traveltimes, raypaths, waveforms and amplitudes are minimally distorted by macro-velocity variations. By the same token, conventional reflection geometries are not optimal if velocity determination is the primary aim. In this case a geometry is required for which traveltimes, raypaths and waveforms are maximally distorted by velocity variations. Geometries that include wide-angle reflections and post-critical turning rays provide such an opportunity.

Wide-angle seismic surveys, often referred to as refraction surveys, are common in scientific projects designed to investigate the middle and lower crust. Such surveys use continuously refracted energy, as well as supercritical reflected energy recorded at up to several hundered kilometres offset, to measure crustal velocities down to many tens of kilometres. Conventionally, wide-angle data are interpreted using ray tracing to fit traveltimes, amplitudes and waveforms subjectively (e.g. McCarthy *et al.* 1991), by inversion of traveltimes only (e.g. Hole, Clowes & Ellis 1992), or by full waveform inversion assuming a 1-D layered earth (e.g. Cary & Chapman 1988). None of these techniques appears sufficient, since all traveltime methods have fundamental resolution limitations, whereas 1-D methods are inadequate in the presence of significant crustal structure. Sun & McMechan (1991, 1992) proposed a full wavefield inversion method for wide-aperture data. While promising, their approach requires significant supercomputing resources. The approach we shall describe in this paper is similar, but is implemented in the frequency domain, and the examples that we show, both real and synthetic, can be computed on ordinary workstations.

Modern crustal wide-angle data are often multi-fold and multi-channel, with densely sampled source and receiver arrays. Such closely spaced data are potentially amenable to multi-channel wavefield techniques, for example migration, and reverse-time propagation. In this paper, we will advocate a '2 1/2-D' wavefield inversion technique that has many features in common with seismic migration. Our method is based on finite-difference modelling of the wave equation, thus allowing very general wave types to be incorporated and enhancing the resolution when compared to traveltime methods. The method operates in the frequency domain, which is efficient when inverting data from a multiplicity of sources, and allows us to model and invert velocity structure as well as near-constant Q inelastic attenuation factors. The inversion can be iterated to improve the data fit and to take account of some non-linearity. To make the method tractable we invert only single frequency components of the data at a time. We mitigate some of the non-linearity by always using starting models that have been developed using more primitive methods (i.e. traveltime analysis), and by initiating inversions using the lowest signal frequencies available.

Our method was developed originally for use with cross-borehole seismic data, and has recently been used successfully on real, but small-scale data (Song, Williamson & Pratt 1994). We now propose to use this method to invert deep refraction arrivals from the middle and lower crust. Unfortunately we are still limited in our synthetic experiments to quite low frequencies. However, several recent advances in finite differencing will allow us to use coarser grids. With the arrival of massively parallel computers we hope soon to solve real 2-D deep-crustal problems.

This paper is organized into three principal sections. We begin by briefly reviewing our results with real cross-borehole data, in order to demonstrate clearly that the methods are feasible and can indeed lead to a significant improvement in resolution of velocity models, when compared with traveltime inversions. We then proceed to review the fundamental forward modelling and inverse theory results that we use to implement the method. We present two simple studies using synthetic data in a wide-angle configuration that demonstrate the imaging principles involved. Finally, we present a more extensive synthetic study based on a real crustal data set collected over the Basin and Range province in south-western USA in order to illustrate the potential of the method for providing velocity models of high accuracy and resolution in a realistic environment.

INVERSION OF REAL CROSS-BOREHOLE DATA

During the previous decade, many explorationists became interested in the potential benefits of seismic tomography using source and receiver arrays deployed in boreholes (e.g. Dines & Lytle 1979; Bregman, Bailey & Chapman 1989a; Pratt & Chapman 1992; Pratt & Sams 1996). This has lead to a number of developments in a field generally referred to as cross-borehole tomography. While logistical problems may prevent the technique from becoming a routine imaging method, much has been learned about the physics and mathematics of imaging with data from experiments with limited tomographic apertures. This experience is relevant to the tomographic reconstruction of velocities from wide-angle crustal data.

Fig. 1 illustrates and compares the primary features of the two different wide-angle surveys we deal with in this paper: the cross-borehole survey and the wide-angle crustal survey. Both surveys interrogate the subsurface using source and receiver spreads that are finite in length and constrained to lie along straight lines at the edges of the target. Both surveys lead to wave propagation that is primarily parallel to the layering of the geological section, and hence contain 'difficult' seismic phases, such as supercritical reflections and refractions, turning rays, and interference head waves. In spite of these similarities, there are significant differences in scale. The cross-borehole survey that we will discuss in this section was carried out across $L = 30$ m of section, using sources with frequencies of the order of 500 Hz. This implies that wavelengths, λ, were of the order of 4 m in the 2 km s^{-1} sediments, and that the width of the first Fresnel zone, given as $\sqrt{\lambda L}$ (e.g. Williamson 1991), is of the order of 10 m. The crustal experiment that we use as an example measures seismic arrivals that have propagated more than 250 km, at much lower frequencies (of the order of 5 to 10 Hz). Given an average crustal velocity of 6 km s^{-1}, this implies wavelengths of the order of 0.5 to 1.0 km, and a width of the Fresnel zone as large as 20 km. The discrepancy between the wavelength and the width of the Fresnel zone is a critical factor in deciding whether or not wavefield inversion, as compared to traveltime inversion, is worth the additional computational cost.

Fig. 2 depicts three images, derived in three different manners from a single set of cross-borehole seismic data. The data were

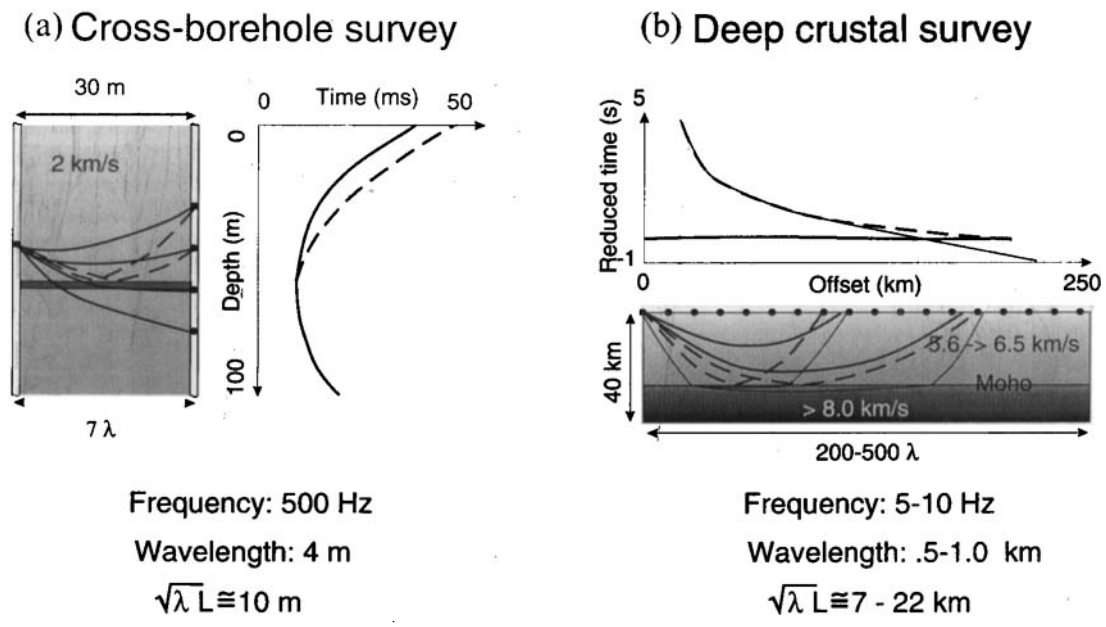

Figure 1. A comparison of survey configurations and characteristic scale lengths for (a) a cross-borehole survey and (b) a deep-crustal survey.

originally acquired by researchers at the University of Durham for the purposes of mapping the continuity of subsurface coal seams; a detailed description of the survey is contained in Findlay, Goulty & Kragh (1991). Each panel is annotated with arrows showing the location within each borehole at which coal seams were encountered. These seams are of anomalously low seismic velocity, with thickness of the order of several metres. It can be seen from Fig. 2 that the seams are offset between the boreholes. From the fact that seam 'z' (containing older sediments) is offset by less than seam 'y', we may infer that either a system of faults must be present, or that, if there is only a single fault, this must be a growth fault.

Panel (a) in Fig. 2 is a pre-stack migration of the data. The particular algorithm used to compute this image is known as the 'Inverse Generalized Radon Transform' (inverse GRT; Miller, Oristaglio & Beylkin 1987); however, the image shares many features in common with a pre-stack image shown in Findlay *et al.* (1991) using a different pre-stack migration algorithm. The image is of sufficient resolution to allow a tentative interpretation of the location of the faulting to be made. Reflections from seams 'y' and 'z' appear continuous in the image and are associated with their intersections with the right-hand edge of the survey, but both reflectors appear to be truncated near the left-hand edge. Seam 'z' extends almost to the left-hand borehole, whereas seams 'y' and 'x' are truncated near the centre of the section. Although an effort was made to respect true amplitudes in the migration, this result is essentially a qualitative, rather than a quantitative, image of the reflectors.

Fig. 2(b) is a tomographic reconstruction of the velocity field using first arrival times and ray-trace techniques (see Williamson 1993a, b). This tomogram is typical of many other cross-borehole tomography results reported in the literature, in that the image is of low resolution. None the less, there are hints of low-velocity zones that are correlated with the reflectors that appear in the pre-stack migration in panel (a). In contrast to the migration of the data, the image can be interpreted quantitatively: the velocities represent smoothed averages of the true rock velocities, where the averaging kernels have approximately the width of the first Fresnel zone.

The final panel, Fig. 2(c), is the result that was recently obtained by Song *et al.* (1994) using the wavefield inversion technique that we are advocating in this paper. When compared with the traveltime tomography in panel (b), there is a dramatic improvement in the resolution. The low-velocity coal seams stand out clearly in the image, with resolutions that are comparable to the pre-stack migration in panel (a). In contrast to the migration, the image is quantitative in terms of velocity. [The wavefield inversion of the real data in Fig. 2(c) required several additional factors to be taken into account: tube waves needed to be removed from the input data; the source amplitude and phase needed to be included separately as variables in the inversion scheme; and anisotropy known to be present needed to be accounted for. These, and other, issues are dealt with further by Song *et al.* (1994).]

We maintain that the significant improvement in resolution that is observed between Figs 2(b) and (c) was achieved because we abandoned the simple concepts of traveltimes and rays, and turned instead to a method that can account for more general wave propagation effects. The tomography result is compatible with the theoretical prediction that the resolution will be of the order of the first Fresnel zone width (10 m in this case). The wavefield inversion is compatible with the prediction (Wu & Toksöz 1987) that this result should have a resolution of the order of half the wavelength (2 m in this case).

The significance of these results with real cross-hole data to the crustal problem may be appreciated with reference to Fig. 1(b). In wide-angle crustal surveys, because some phases are transmitted over very long path lengths, the width of the first Fresnel zone can be surprisingly large (up to 20 km in this example). Without resort to additional (*a priori*) information, reconstructions from transmission traveltimes alone will be of exceedingly poor resolution. Wavefield inversion offers a way in which the resolution of the reconstructions can be dramatically improved to the more acceptable scale lengths of half the

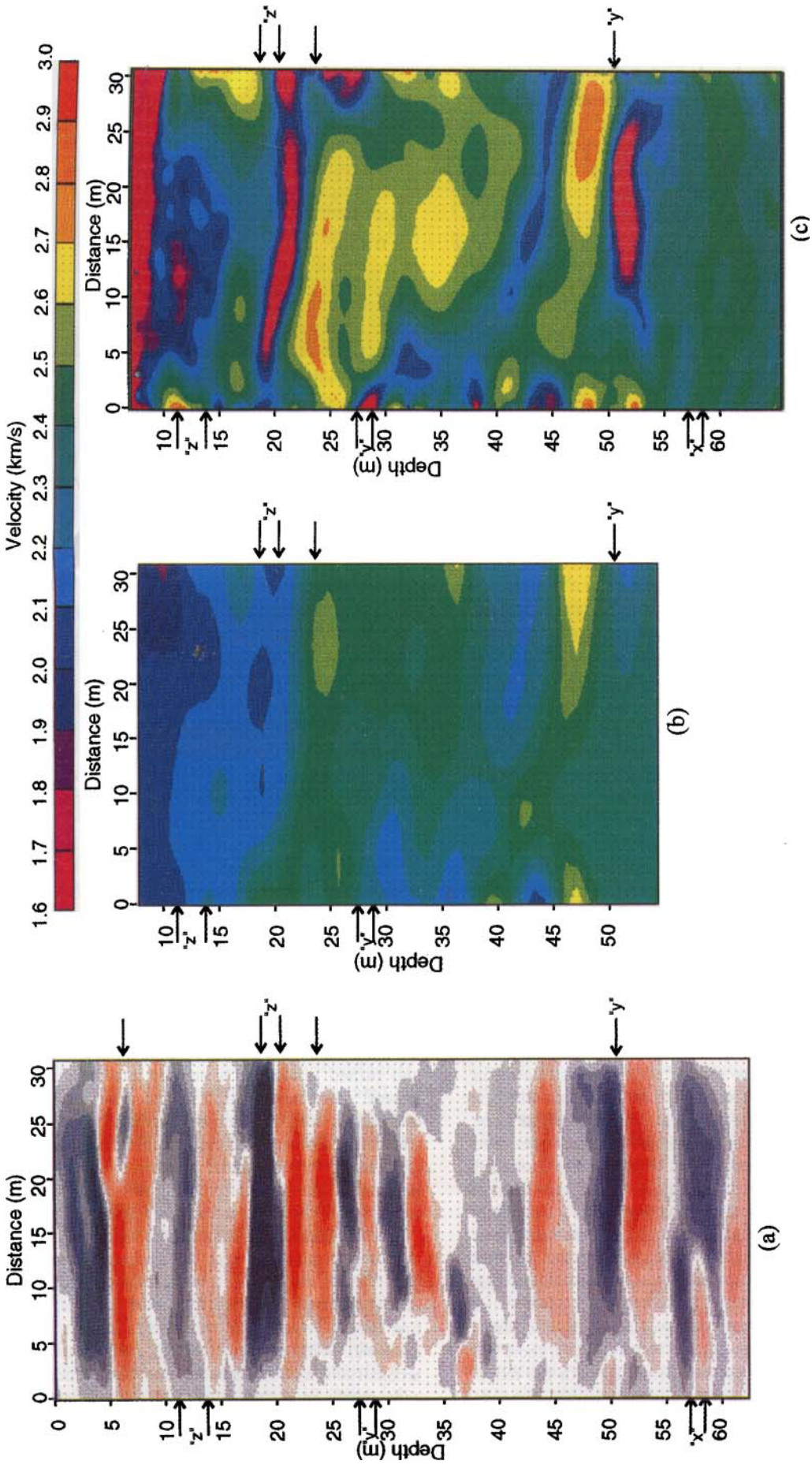

Figure 2. (a) Pre-stack migration image (inverse GRT) obtained using cross-borehole seismic data acquired in a near-surface sedimentary sequence containing several coal seams. The locations of the coal seams within each of the two boreholes are marked by arrows. (b) Traveltime inversion of the same crosshole data. (c) Wavefield inversion of the same crosshole data. Four discrete frequency components of the data (200, 300, 400 and 500 Hz) were used to form image (c).

wavelength (of the order of 0.5 km in this example). There is a practical consideration here: the size of wide-angle surveys, in terms of wavelengths, is much greater than the real cross-borehole survey described above (see Fig. 1). This leads to difficulties in fitting these larger models into core memory on computer workstations. Either the methods must be made more efficient, or we must turn to large-scale computing platforms. For this reason, a later section of this paper will use a low-frequency numerical simulation of a wide-angle crustal survey in order to demonstrate the potential benefits. But before proceeding to this demonstration, the next section will elaborate on the mathematics that underlie the method, and graphically demonstrate some of the imaging principles that are involved.

METHOD

At the core of the imaging method that was used to construct Fig. 2(c) lies a numerical solution to the acoustic wave equation by the method of finite differences. The finite-difference method generates all possible wave types within a given model, and can be used to simulate very complex seismic wavefields. By the same token, the complexity of the wavefields makes these almost as difficult to interpret as real seismic data, although tools such as ray tracing and time slicing can be used to supplement the simulations. However, we shall not be concerned with interpreting the wavefields, only with using them in an automatic inversion scheme.

All work presented in this paper is based on the acoustic approximation, rather than on the more complete elastic wave equation. This makes the mathematics simpler, the computer software is then less complex, and larger models may be run. The approximation appears sufficient for the real cross-borehole data presented earlier, in part due to the large Poisson's ratio of the sediments involved. However, we recognize the importance of using an elastic wave equation, and we are currently concentrating our research efforts towards developing the equivalent algorithms for the elastic (and possibly anisotropic) wave equation. Indeed, some work on the elastic wave equation already exists (see Pratt 1990a,b for examples).

We choose to implement the method entirely in the frequency domain. This has the following implications.

(1) The successive solution of the forward problem for large numbers of source locations is computationally efficient. We elaborate on this point in the section that follows.

(2) By operating on the discrete frequency components of the data we have a very effective way of 'decimating' the data. Instead of inverting for many time samples of traces from many source–receiver pairs, we utilize only a limited number of frequency components from the same number of source–receiver pairs. In the real data example shown earlier, the image in Fig. 2(c) was computed by inverting sequentially only four frequency components of the data.

(3) Wavefield inversion is a notoriously non-linear problem. By concentrating on lower frequencies initially, this difficulty is mitigated. However, the problem often remains strongly non-linear, and in practice good starting models, usually based on traveltime inversions, are essential.

(4) Frequency-domain simulations allow arbitrary frequency dependence of seismic attenuation factors to be incorporated trivially, and at no extra computational cost. More significantly, the attenuation behaviour of the medium may also be inverted for. However, in order to estimate accurately these inelastic effects it is necessary to use a version of the 2-D finite-difference method that accurately models geometrical effects. This is accomplished using a '2 1/2-D' method, as described below. For the real cross-borehole example, images of the distribution of the attenuation factor, Q, were also computed (these are not shown here, but they are presented in Song *et al.* 1994). While several authors have attempted to use amplitude information to recover attenuation tomograms (e.g. Bregman, Chapman & Bailey 1989b), wavefield inversion yields much more accurate and better resolved images than any ray-based method (for comparisons on synthetic data we refer the reader to Pratt, Song & Williamson 1994).

The forward problem

We begin with the 3-D, constant-density acoustic wave equation, for a single frequency, ω, given a point source at Cartesian coordinates (x_s, y_s, z_s):

$$\left(\nabla_3^2 + \frac{\omega^2}{c^2(x, y, z)}\right) P(x, y, z; \omega) = -S(\omega)\delta(x|x_s)\delta(y|y_s)\delta(z|z_s), \tag{1}$$

where $P(x, y, z; \omega)$ is the (complex valued) pressure field to be found, $S(\omega)$ is the Fourier transform of the source-time behaviour and ∇_3 is the 3-D Laplacian operator.

In order to proceed without resorting to full 3-D modelling, which is expensive and unnecessary, we invoke the '2 1/2-D' assumption that all sources and receivers are coplanar at $y_s = 0$ and that the velocity field is constant perpendicular to this sagital plane, so that $c(x, y, z) = c(x, z)$. This allows a spatial Fourier transformation to be applied to eq. (1) in the y direction, yielding the following 2-D equation:

$$\left(\nabla_2^2 + \frac{\Omega^2}{c^2(x, z)}\right) \tilde{P}(x, z; \omega; k_y) = -S(\omega)\delta(x|x_s)\delta(z|z_s), \tag{2}$$

where $\tilde{P}(x, z; \omega; k_y)$ is the k_y wavenumber component of the pressure field, ∇_2 is the 2-D Laplacian operator, and Ω is related to the frequency and the wavenumber by

$$\Omega^2 = \omega^2 - c^2(x, z)k_y^2. \tag{3}$$

A discrete approximation to the continuous wave eq. (2) can be generated by the method of finite differences (or, alternatively, the method of finite elements; see Marfurt 1984 for a comparison). This leads to the matrix equation

$$[\mathbf{K} + \mathbf{M}(\omega; k_y)]\tilde{\mathbf{p}}(\omega; k_y) = -\mathbf{s}(\omega), \tag{4}$$

in which the large, sparse matrices $\mathbf{K}$ and $\mathbf{M}$ replace the Laplacian and Ω^2/c^2 terms in the continuous equation, and the vectors $\tilde{\mathbf{p}}$ and $\mathbf{s}$ replace the continuous field and source terms. Once this equation has been solved for a sufficient number of wavenumbers, the desired field quantity at $y = 0$ can be constructed using the wavenumber summation

$$\mathbf{p}(\omega, y = 0) = \frac{1}{2\pi}\sum_{k_y} \tilde{\mathbf{p}}(\omega; k_y)\Delta k_y. \tag{5}$$

There are various issues involved with the selection of an appropriate range of k_y values in order to obtain accurate amplitudes and phases. These have been discussed by Song &

Williamson (1994). For the real-data example given earlier, 40 separate wavenumber solutions contributed to each frequency component.

The matrix equation (5) can be solved using a variety of techniques. Iterative methods conserve memory but require new solutions to be generated separately for each right-hand side (i.e. for each new source in the survey). Direct methods are expensive in terms of memory requirements, but have the advantage of allowing additional sources to be incorporated at marginal extra costs. We utilize the direct method of LU decomposition. In order to conserve memory it is critical to use an optimal ordering of the nodal points and to retain the sparsity of the resultant factored matrices. We reorder the nodal points using the nested dissection method of George & Lui (1981).

Born-approximation 'wavepaths'

Woodward (1992) introduced the term 'wavepath' to the seismic imaging problem as a useful concept for understanding the physical meaning of both Born and Rytov approximations. Here we use this concept to provide a link between the forward modelling problem and the inverse problem, and also to elucidate the imaging limitations of the wide-angle problem. Woodward expressed the Born approximation for acoustic waves as

$$\delta P(\mathbf{g}|\mathbf{s};\omega) = \int \frac{\delta c(\mathbf{r})}{c_0(\mathbf{r})} \mathscr{L}_0(\mathbf{r},\mathbf{g}|\mathbf{s};\omega)\, d\mathbf{r}. \tag{6}$$

Eq. (6) predicts perturbations to the wavefield for a given source–receiver pair (at locations **s** and **g**) for small perturbations $\delta c(\mathbf{r})$ in the 'background' velocity field, $c_0(\mathbf{r})$. When the incident waves originate from point sources, $\mathscr{L}_0(\mathbf{r},\mathbf{g}|\mathbf{s};\omega)$ is an averaging kernel given by

$$\mathscr{L}_0(\mathbf{r},\mathbf{g}|\mathbf{s};\omega)\, d\mathbf{r} = 2\frac{\omega^2}{c_0^2(\mathbf{r})} G_0(\mathbf{g}|\mathbf{r};\omega) G_0(\mathbf{s}|\mathbf{r};\omega) \tag{7}$$

(i.e. the product of two Green's functions in the background medium, one centred on the source location, and one centred on the receiver location). Woodward compared this formalism to a similar formalism in which the integrating kernel for traveltime perturbations is given by the ray path linking the source–receiver pair, and hence she termed $\mathscr{L}_0(\mathbf{r},\mathbf{g}|\mathbf{s};\omega)$ the 'Born-approximation wavepath'.

In Fig. 3 we depict the real parts of the terms $G_0(\mathbf{g}|\mathbf{r})$, $G_0(\mathbf{s}|\mathbf{r})$ and $\mathscr{L}_0(\mathbf{r},\mathbf{s}|\mathbf{r})$ for a representative wide-angle seismic problem. In Fig. 3 the background velocity field $c_0(\mathbf{r})$ is a 1-D linear increase in velocity from 6 km s^{-1} at the surface to 6.7 km s^{-1} at 40 km depth. This velocity gradient is just sufficient to cause seismic rays for the maximum offset of 250 km to turn at the 40 km base of the model. The single frequency used to compute these functions was 0.5 Hz. The wavepath contains characteristic distorted elliptical lobes. Woodward showed, by examining similar wavepaths for the Rytov linearization, that the first lobe (the one centred on the equivalent ray path) yields contributions to the perturbed wavefield that reach the receiver within half a wavelength of the source wavefield. Hence, this lobe can be considered to be roughly equivalent to the first Fresnel zone. Using similar wavepaths constructed for the time domain problem, Woodward showed that the outer lobes sample parts of the model that contribute arrivals at ever increasing times. These outer lobes have shapes that corresponds to seismic 'isochrons', as defined by Miller *et al.* (1987).

Just as in ray-based tomography, in which we backproject traveltime errors along ray paths, we can reconstruct velocity anomalies by projecting the complex-valued frequency components of the wavefield errors for the current model over these wavepaths. The wavenumber content of a given reconstruction will depend on which part of the source–receiver wavepaths for the experiment illuminate the anomaly. Clearly, if the anomaly falls outside all such first Fresnel zones, the reconstruction will contain little in the way of low wavenumbers. From the arguments of the previous paragraph, errors in the phase at the receiver array due to small differences in the transmitted field will sum coherently within the first Fresnel zone when backpropagated, leading to tomography-like reconstructions. In contrast, we expect that errors in the later part of the wavefield will be responsible for a coherent summation of the isochronal outer lobes of the wavepaths, and hence provide migration-like reconstructions. We shall return to this dual behaviour of the reconstruction algorithm when we interpret the synthetic results in later sections. [It is also possible for Fresnel zones to be associated with reflection events. If this is the case, the reflections will illuminate shallower velocity anomalies and provide additional constraints on the lower wavenumbers. In order for this to occur, the current velocity model must generate these reflections, and the amplitudes must be large enough to contribute to the inversions. Schemes for forcing similar inversion methods to use reflection energy were the subject of much study by Mora (1987b) and others.]

Inverse method

The previous section summarized our approach to solving the forward problem: given a velocity model, predict a synthetic wavefield that can be compared to the observed wavefield. In this section we summarize how these wavefield predictions may be used to update the velocity model iteratively, in order to reduce the differences between the synthetic and observed wavefields.

The general approach we use is similar to that used by many other authors, including Lailly (1984), Tarantola (1984, 1987), Mora (1987a, 1988) and Beydoun & Mendes (1989). For a velocity model specified by a vector **c**, consisting of velocities at the nodal points of a finite-difference grid, we may define the least-squares objective function, or cost function (i.e. a measure of the misfit of the data), in the current model as

$$S(\mathbf{c}) = \frac{1}{2}\|\mathbf{P}_{\text{obs}} - \mathbf{P}_{\text{mod}}\|^2 \equiv \frac{1}{2}\|\delta\mathbf{P}\|^2, \tag{8}$$

where $\mathbf{P}_{\text{obs}}$ and $\mathbf{P}_{\text{mod}}$ are the discrete observed and modelled wavefields arranged as vectors, and $\|\ \|$ represents an appropriate Euclidean norm. If the data space is also discrete, and we choose to define the Euclidean norm using the covariance matrix of the data, $\mathbf{C}_p$, we may write

$$S(\mathbf{c}) = \frac{1}{2}\delta\mathbf{P}^\dagger \mathbf{C}_p^{-1} \delta\mathbf{P}, \tag{9}$$

(the symbol † is used to denote the Hermitian transpose). In solving inverse problems one would like to minimize this objective function. For general wavefield inverse problems such an objective function is likely to be exceedingly complex and

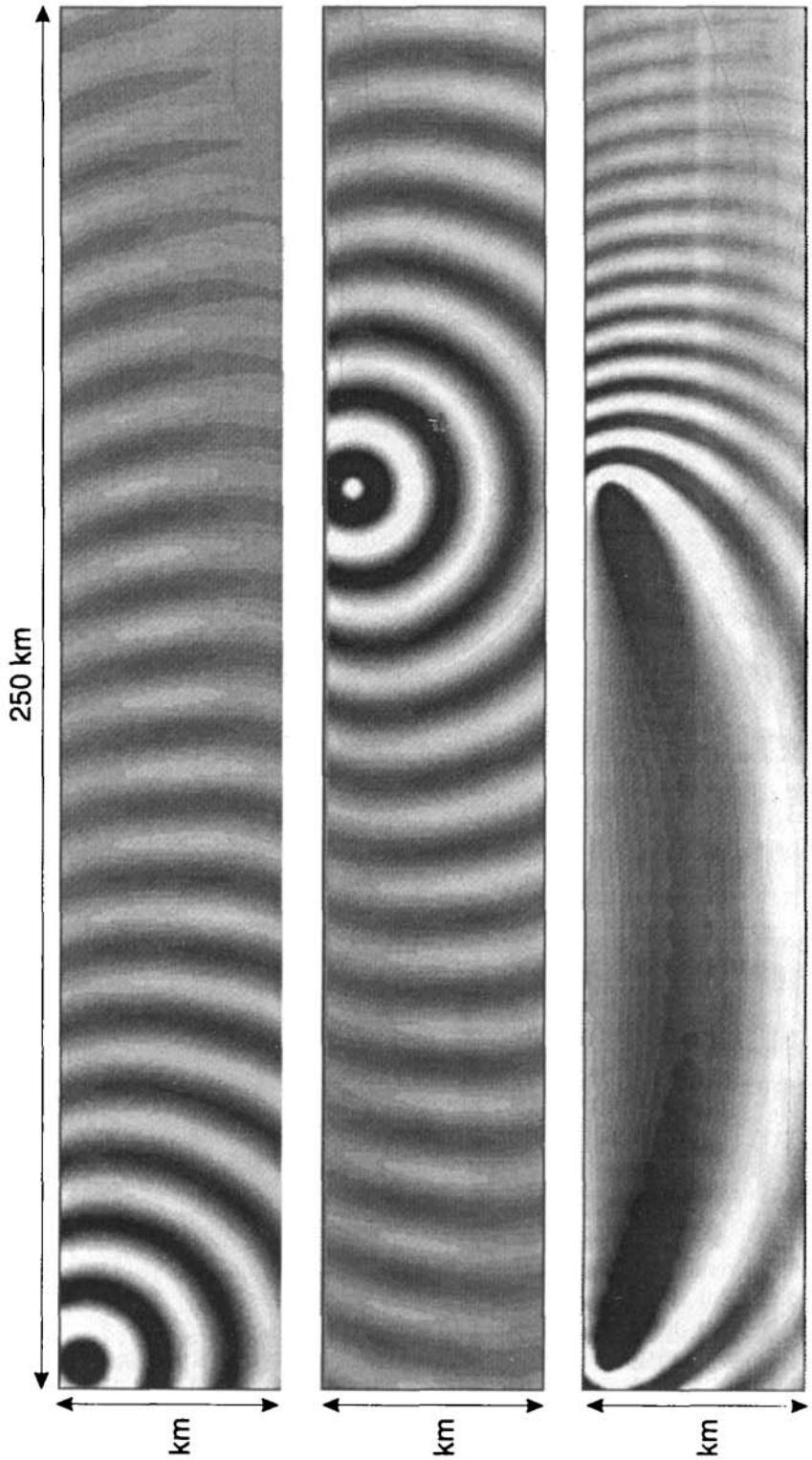

Figure 3. An illustration of Woodward's (1992) concept of a Born approximation 'wavepath' for the analysis of deep-crustal data. (a) A source Green's function. (b) A receiver Green's function. (c) The Born approximation wavepath for this particular source–receiver pair.

Figure 3. An illustration of Woodward's (1992) concept of a Born approximation 'wavepath' for the analysis of deep-crustal data. (a) A source Green's function. (b) A receiver Green's function. (c) The Born approximation wavepath for this particular source–receiver pair.

to contain many local minima, due to the highly non-linear dependence of the data residuals on the velocity parameters. Rather than simply minimizing such a function, ideally one would like to characterize its global behaviour. Unfortunately, due to the size of the velocity-parameter space and due to the computational cost of the forward problem, we have little choice but to resort to the use of local information to descend to the nearest local minimum. This implies a strong dependence on initial, less rigorous and more robust methods (such as traveltime inversion) to define starting models that lie in the region of the global minimum. The final solution may then be sought by computing the gradient of $S(\mathbf{c})$ with respect to the independent variables $\mathbf{c}$:

$$\hat{\mathbf{g}} = \nabla_c S(\mathbf{c}) = -\mathbf{L}^\dagger \mathbf{C}_p^{-1} \delta \mathbf{P} \tag{10}$$

(Tarantola 1987), where $\mathbf{L}^\dagger$ is the adjoint of the Frechét derivative matrix, $\mathbf{L}$, for the linearized forward problem,

$$d\mathbf{P} = \mathbf{L}\delta\mathbf{c}, \tag{11}$$

which corresponds to a discrete version of the Born approximation. The matrix $\mathbf{L}$ contains the collective behaviour of the Born approximation wavepaths for all source–receiver pairs in the data set.

The steps by which the action of the adjoint of the Frechét derivative matrix on the data residuals [i.e. eq. (10)] may be established through use of the linearized forward problem [eq. (11)] are well known (see the various papers cited at the beginning of this section). For the specific forward problem of 2 1/2-D modelling in the frequency domain, the gradient may be computed from the data residuals using

$$\hat{\mathbf{g}} = \delta\hat{\mathbf{c}}(\mathbf{r}) = \frac{\omega^2}{2\pi c_0^3(\mathbf{r})} \sum_{k_y} \Delta k_y \sum_s P_b(\mathbf{r}|\mathbf{s}, k_y) P_0^\dagger(\mathbf{r}|\mathbf{s}, k_y) \tag{12}$$

(Song, Williamson & Pratt 1994a), in which the forward propagated field is given by

$$P_0(\mathbf{r}|\mathbf{s}, k_y) = S(\omega) G_{2\,1/2}(\mathbf{r}|\mathbf{s}, k_y), \tag{13}$$

the 'backpropagated field' $P_b(\mathbf{r}|\mathbf{s}, k_y)$ is given by

$$P_b(\mathbf{r}|\mathbf{s}, k_y) = \sum_g \delta\hat{P}(\mathbf{g}|\mathbf{s}) G_{2\,1/2}^\dagger(\mathbf{r}|\mathbf{g}, k_y), \tag{14}$$

and the weighted data residuals are given by

$$\delta\hat{P}(\mathbf{g}|\mathbf{s}) = \mathbf{C}_p^{-1} \delta P(\mathbf{g}|\mathbf{s}). \tag{15}$$

In eqs (13) and (14), $G_{2\,1/2}(\mathbf{r}|\mathbf{s}, k_y)$, is the '2 1/2-D' Green's function, dependent on both frequency and wavenumber, defined as the solution to eq. (2), with a unit source term on the right-hand side.

The operations implied by eqs (12), (13), (14) and (15) may be summarized in the following manner.

(1) Compute data residuals for each source–receiver pair by computing the synthetic data in the current model using eqs (4) and (5) and subtracting the resultant wavefields from the corresponding frequency component of the observed data. Because of the use of a direct solution method for solving eq. (4), additional source locations are incorporated at marginal extra cost, and we are thus able to carry out these computations for a large number of source–receiver pairs.

(2) For each wavenumber and each source form a backpropagated field by multiplying the weighted data residuals [eq. (15)] for each source–receiver pair with the corresponding conjugated 2 1/2-D Green's function, summing the results over all receivers [as in eq. (14)]. Due to the linearity of the operation, it is not actually necessary to compute individual 2 1/2-D Green's functions—significant savings may be realized by combining all conjugated receiver residuals for each source into a single distributed source term and computing the resultant wavefield.

(3) Combine each backpropagated wavefield with the corresponding conjugated modelled field by multiplication [eq. (12)].

(4) Carry out computations 2 and 3 for each source (inner loop) and for each wavenumber (outer loop), summing the results as they are obtained. These backward and forward propagations may be carried out for each wavenumber using the same direct solution to eq. (4), and thus have the same marginal cost of the additional forward propagations of step 1 above.

Finally, the gradient vector is scaled appropriately, using a covariance matrix $\mathbf{C}_m$ for the model parameters, and used to update the model using the standard iterative formula

$$\mathbf{c}^{(i+1)} = \mathbf{c}^{(i)} - \alpha_i \mathbf{C}_m \delta\hat{\mathbf{c}}^{(i)}, \tag{16}$$

where α is a step length that may be computed using the well-known (linear) formula (Tarantola 1987). The simple gradient need not be used; conjugate gradients may also be computed (e.g. after Polak & Ribiére 1969) and used instead, to increase the rate of convergence. A line search may be required to ensure that the correct step length is used in such non-linear problems. Once a new model is obtained using eq. (16), the entire process may be repeated until some convergence criterion is satisfied.

SYNTHETIC EXAMPLES

It is useful to illustrate the principles of the previous section with examples that make the imaging scheme clear. In this section we choose two models that will highlight, respectively, the tomography-like and the migration-like aspects of the method. Both models use the same background velocity model used to generate the wavepath shown in Fig. 3, i.e. a 1-D linear gradient starting at 6 km s^{-1} at the surface and rising to 6.7 km s^{-1} at 40 km depth. In all cases we use a surface array of 240 receivers with a 1 km interval. We begin by studying the single-source inverse problem for both experiments, which is instructive, but yields poorly resolved reconstructions. We then proceed to using 12 surface sources with a 20 km shot interval, which yields much better resolved reconstructions. The experiments were carried out at 0.5 Hz, so that the wavepath from Fig. 3 is directly relevant to the examples. Rather than use full 2 1/2-D modelling and inversion, we have saved computer time by carrying out all simulations only in 2-D, since Song *et al.* (1995) have shown that comparative tests using both methods yield similar results (however, note that in the case of real data, it is essential to use 2 1/2-D methods).

The first model (Fig 4) consisted of a rectangular anomaly 10 km deep and 40 km wide at mid-crustal depths, in which the velocity was held constant. As the background velocity increases linearly with depth, the top half of the perturbation is positive, while the bottom half is negative. Maximum perturbations were 65 m s^{-1}. Since this anomaly is well illuminated by the first Fresnel zone in the wavepath shown in

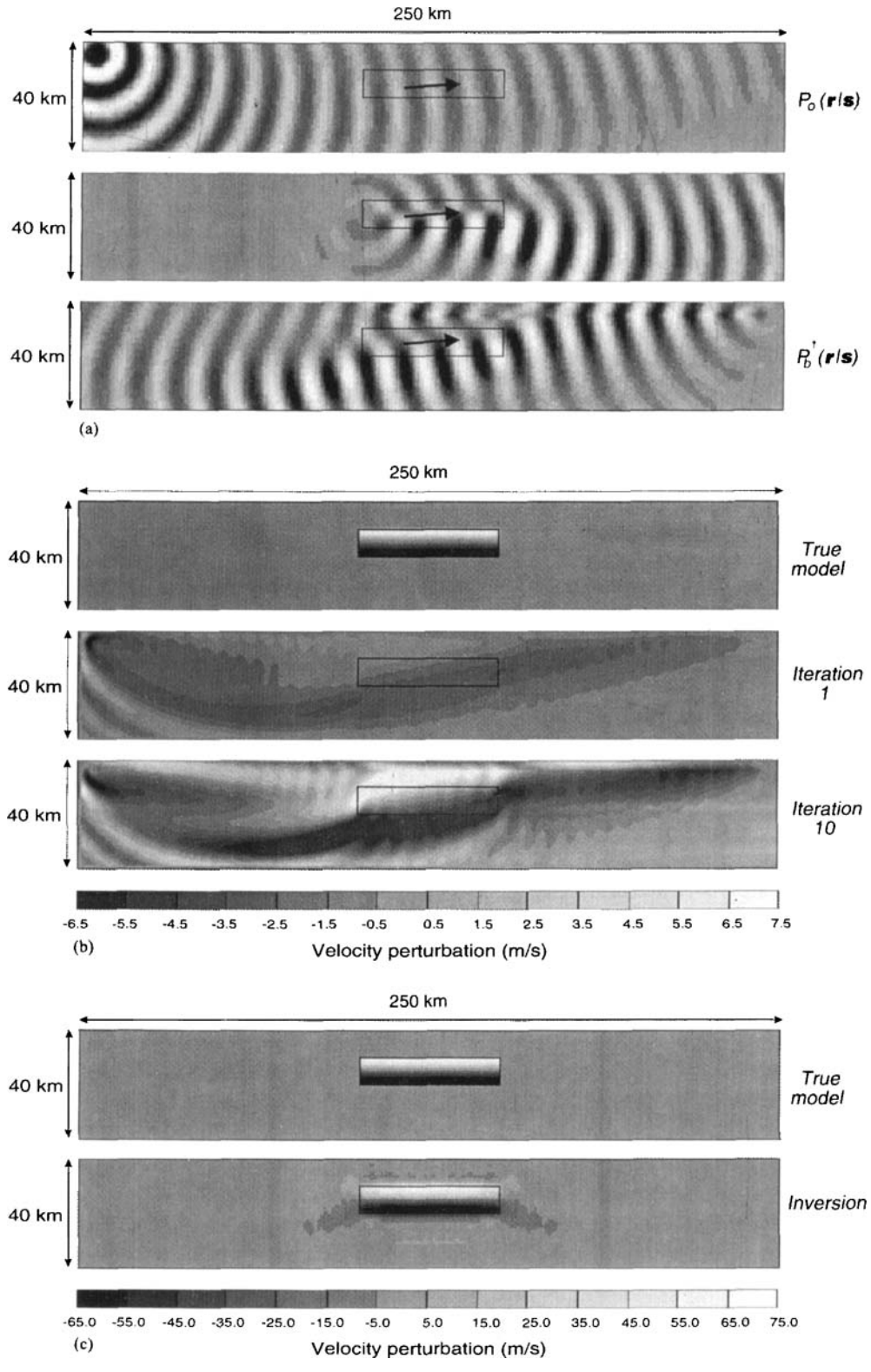

Figure 4. A graphical illustration of the imaging/inversion method employed. A single source and 240 receivers spread evenly across the surface are used. (a) The forward propagated term in eq. (12), $P_o(\mathbf{r}|\mathbf{s})$ (top panel), is combined with the backpropagated residuals, $P_b^{\dagger}(\mathbf{r}|\mathbf{s})$ (bottom panel), to form an image for each source position (see Fig. 5). The central panel is the 'difference wavefield', due to the presence of the rectangular anomaly. Although the difference wavefield is not measured in practice, $P_b^{\dagger}(\mathbf{r}|\mathbf{s})$ is an estimate of the wavefield, obtained by backpropagating the data residuals (from all 240 surface receivers simultaneously) into the model. (b) Images of the rectangular anomaly using all 240 receivers, but only a single source and a single frequency component. The top panel is the true anomaly, the central panel is the initial iteration (gradient image) and the bottom panel is the reconstruction after 10 iterations. (c) Images of the rectangular anomaly using 12 surface sources (spread evenly at 20 km intervals along the top of the model), 240 surface receivers and three frequency components (0.5 Hz, 1.0 Hz and 2.0 Hz).

Fig. 3, we may expect a tomography-like reconstruction of the anomaly. The second model (Fig. 5) consisted of a high-velocity slab anomaly with an increase of 3 km s^{-1} in the bottom 10 km of the model. As the slab is illuminated essentially by the outer lobes of the wavepath in Fig. 3, we may expect a migration-like reconstruction of this anomaly. The following paragraphs will make this distinction between the reconstructions clear by showing some of the intermediate steps in the reconstruction process.

Fig. 4(a) shows the real components of three wavefields in the rectangular anomaly model: the top panel is the forward-propagated wavefield in the background model, the central panel is the difference wavefield computed by subtracting the wavefield in the top panel from the wavefield computed when the perturbation was introduced, and the bottom panel is the backpropagated wavefield, summed over all receivers for the given source. The top panel thus represents $P_0(\mathbf{r}|\mathbf{s})$ in eq. (12) and the bottom panel represents $P_b^\dagger(\mathbf{r}|\mathbf{s})$, both of which may be computed for real inversion problems. The difference wavefield in the central panel cannot be computed without a knowledge of the true perturbation, but it is instructive to compare this with the backpropagated field.

Arrows are plotted in the region of the anomaly for the three wavefields in Fig. 4(a). The arrows represent the gradient direction of the phase of the forward-propagated field, the difference field and the *conjugate* of the backpropagated field. The significance of this is that, for this configuration, both $P_0(\mathbf{r}|\mathbf{s})$ and $P_b^\dagger(\mathbf{r}|\mathbf{s})$ have essentially the same phase gradient at this location. Thus the two phases cancel when multiplied using eq. (12) (i.e. the peaks and troughs of the two wavefields are aligned), and there is a large region of the model in which the phase of the product field varies only slowly. Thus, an image is formed that is similar to a tomographic backprojection of the residuals. We can observe this on the actual images for the single source involved, shown in Fig. 4(b), after just one iteration and after 10 iterations. The image of the anomaly is a 'smeared' version of the true anomaly, where the smear corresponds to the region over which the forward- and back-propagated wavefields are in phase. After 10 iterations the magnitude of the velocity perturbation on the image has grown to approximately 7 m s^{-1}, which is but a fraction of the true velocity anomaly, due to the redistribution of the anomaly over the larger region. The true velocity anomaly may be recovered by using additional source locations to obtain the necessary angular coverage of the anomaly. Fig. 4(c) depicts the reconstruction using 12 sources evenly distributed along the surface. This reconstruction shows the resolution that may be expected from such multi-source data; the anomaly (which has a characteristic size of the order of a half-wavelength) is well resolved. In the computation of the image in Fig. 4(c) three frequencies were used in succession: 0.5 Hz, 1 Hz and 2 Hz.

The experiment is repeated in Fig. 5 for the high-velocity slab amomaly. Fig. 5(a) shows that, in this case, the forward- and backpropagated fields do not propagate in the same direction at the anomaly. This is because the wavefield perturbation that is recorded at the receiver array is essentially a backscattered (mainly reflected) field, rather than a forward-scattered, transmitted field. Because the two fields propagate in different directions, the fields are only in phase at the interface, and hence the resultant reconstruction will only be significant at this location. This is evident in Figs 5(b) and (c), in which the reconstructions for a single source and for multiple-source locations are shown. The final reconstruction using 12 source locations and three frequencies in Fig. 5(c) fails to reconstruct the 3 km s^{-1} magnitude of the perturbation, but the location of the interface and the polarity of the discontinuity are correctly recovered. Just as in seismic migration, the discontinuity is imaged, but the low-wavenumber components are missing. This may be traced back to the central panel of Fig. 5(a), in which the forward-scattered component of the difference field is seen to propagate to the right-hand edge of the model, beyond the range of the receivers. Without this forward-scattered component, the reconstructions cannot be tomography-like.

In this section we have compared situations in which the reconstructions are tomography-like with situations in which the reconstructions are migration-like. The key concept was a comparison of the phase gradients of the forward-propagated wavefield and the conjugate of the backpropagated wavefield. This concept is not ours—it was pointed out much earlier by Mora (1987b). We have shown that the two aspects of inversion, which Mora showed separately for the two cases of surface reflection data and crosshole data, can both be found in the case of a single wide-angle surface survey. Mora's demonstration was given for time-domain inversion (in which the relevant concept is not the phase gradient but the local propagation direction), whereas we showed an equivalent demonstration for frequency-domain inversion.

Computational considerations

In the simulations used in this section, we have used a maximum frequency of 2 Hz. This upper limit reflects the maximum size of the finite-difference grids that we can currently fit into core memory on the workstation we are using. Using nested dissection and sparse storage algorithms, we require close to 100 Mbytes of core memory for a grid containing $1000 \times 160 = 160\,000$ node points, which is used to represent the 250 km × 40 km model. We used a five-point finite-difference scheme which requires of the order of 10 grid points per wavelength. Therefore we can fit at most 100 wavelengths into the grid, hence the smallest wavelength we can model is 2.5 km. In 6 km s^{-1} rocks this corresponds to 2.4 Hz. We note, however, that recently Jo, Shin & Suh (1994) have given a nine-point per wavelength for the same degree of accuracy and at essentially the same computational cost. Initial tests that we have carried out indicate that we may be able to increase this frequency to 5 Hz using this new scheme. Using additional core memory would allow us to increase this upper limit further.

Our method is memory bound. We can factor eq. (4) for this model size in a few minutes, provided the result is stored in core. As soon as we are required to segment the matrices and use disk storage, we observe drastic increases in execution times due to the slow access times for disk storage.

A CRUSTAL MODEL

The previous section depicted the reconstruction of two somewhat-idealized anomalies. While such tests provide useful insight into the performance of the inversion algorithms, it is also instructive to invert synthetic data from as realistic a situation as possible. Fig. 6(a) shows a model published by

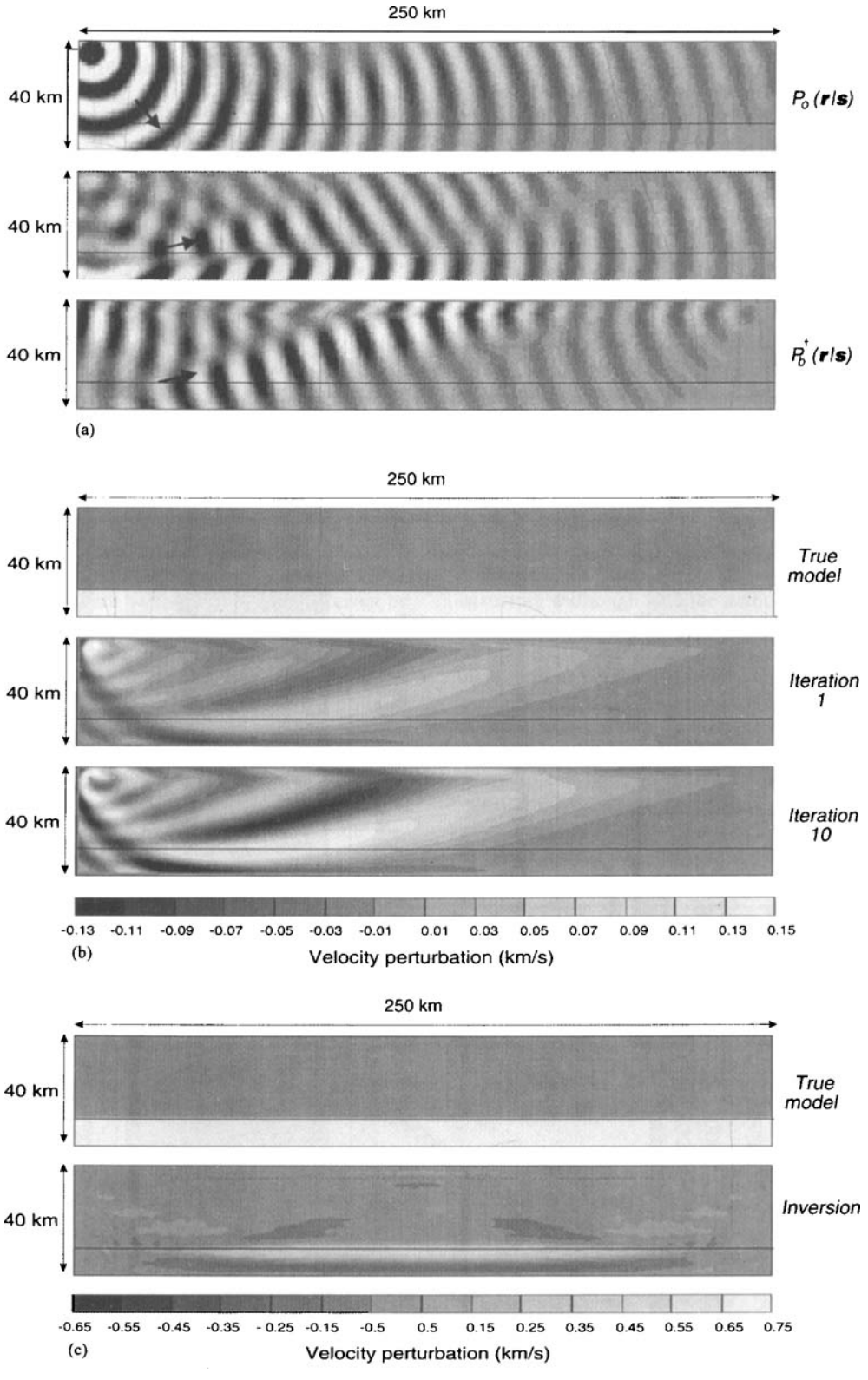

Figure 5. As in Fig. 4, a graphical illustration of the imaging/inversion method employed, but in this case the anomaly is a high-velocity slab at the bottom of the model. (a) Forward-propagated, difference, and backpropagated fields. (b) Images of the slab anomaly using all 240 receivers, but only a single source and a single frequency component. The top panel is the true anomaly, the central panel is the initial iteration (gradient image) and the bottom panel is the reconstruction after 10 iterations. (c) Images of the slab anomaly using 12 surface sources, 240 surface receivers and three frequency components (0.5 Hz, 1.0 Hz and 2.0 Hz).

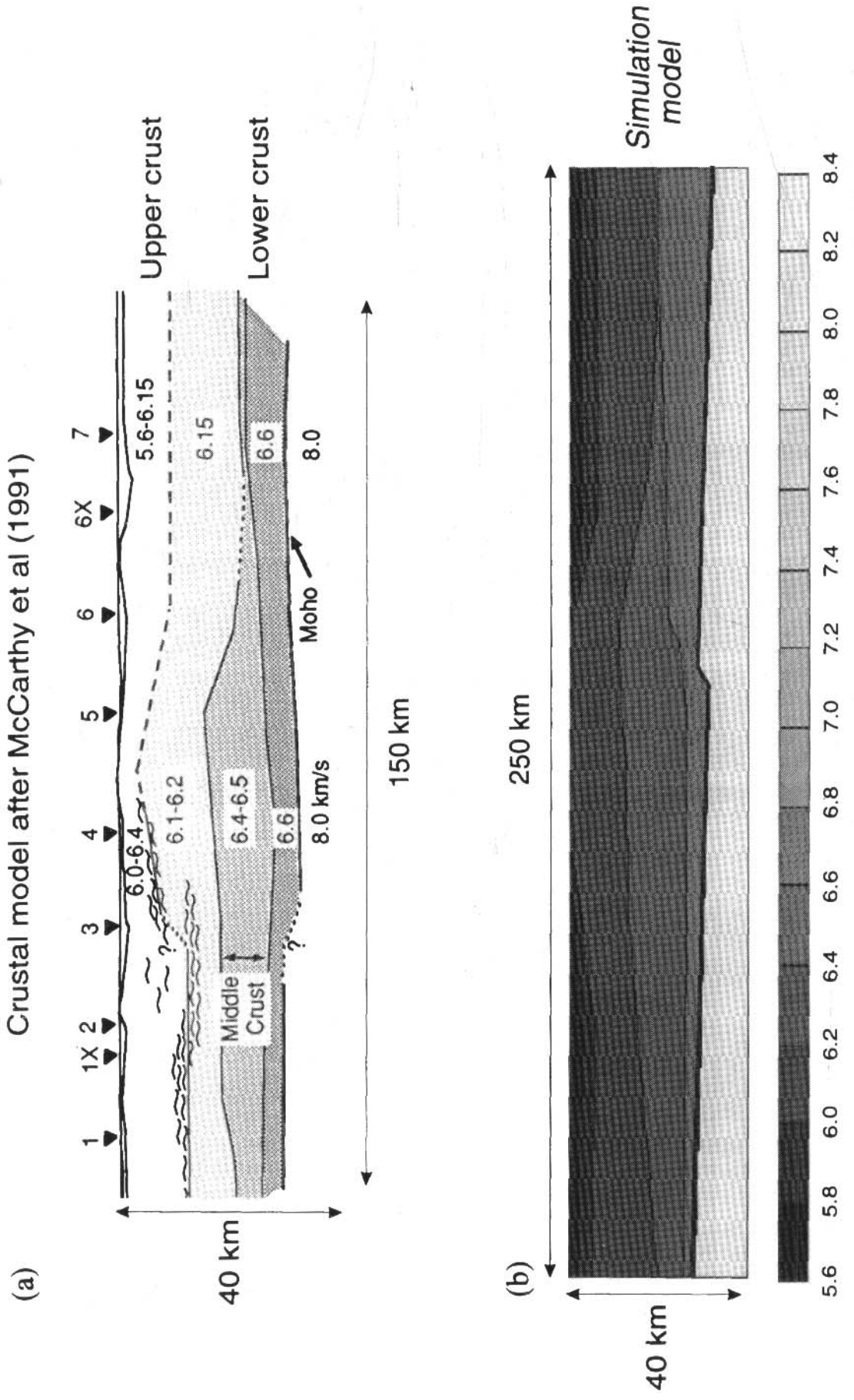

Figure 6. A crustal model derived from a large wide-angle survey in south-western California and western Arizona. Triangles indicate the locations of shot points used. (a) Original model from McCarthy *et al.* (1991). (b) 'Generic' crustal model used in the simulation.

McCarthy *et al.* (1991), based on extensive wide-angle seismic data collected over the margin between the Basin and Range province and the Colorado Plateau in south-eastern California and western Arizona. In Fig. 6(b) we show a model that contains many of the features of the McCarthy *et al.* model. In this section we shall use the model in Fig. 6(b) as a test case for the inversion of wide-angle crustal data. Our model contains a (fictional) discontinuity on the Moho that was included to enable an evaluation of the resolution of the reconstruction at this depth to be made. We conducted a simulated wide-angle survey using 12 surface sources with a shot interval of 20 km and recorded synthetic data in 240 surface receivers (with an interval of 1 km). Again, we considered it sufficient to carry out the experiment in 2-D, rather than in 2 1/2-D.

We computed a complete set of synthetic data for the crustal model in Fig. 6(b) by using the acoustic frequency-domain modelling algorithm described earlier, summing over all frequency components to yield time-domain data. A representative shot record plotted in reduced time is shown in Fig. 7. The phases identified schematically on Fig. 1(b) can be clearly seen. Less obvious are reflections from within the crust, which can be identified on alternative data displays (not shown). These synthetic data compare well with the real data given by McCarthy *et al.*, but are clearly of lower frequency. Using our existing hardware, incorporating the finite-difference scheme of Jo *et al.* (1994), we will probably be able to double the maximum frequency from 3 Hz to 6 Hz, which would bring us into a realistic range. However, if we were to use the elastic wave equation version of the modelling software, we would be constrained to the lower frequencies. Further progress is only possible with more advanced computer hardware, which was not available to us at the time of computing these results.

The inversion of the synthetic data from all 12 sources was straightforward. We decided to use a 1-D starting model that contained the approximate crustal velocity gradient and the appropriate velocity discontinuity at the (constant) depth of 30 km. For these synthetic tests it was not necessary to include the source parameters in the inversions, but, on the basis of synthetic work by Song *et al.* (1994a), we do not anticipate much degradation of the images if this were done. We also omitted finite Q from the forward and inverse computations in order not to complicate the issues. We initiated the inversion with the 0.5 Hz component of the data, then progressed to 1.0 Hz and finally 2.0 Hz. At each frequency 10 iterations of the conjugate gradient method were carried out. The resultant velocity reconstructions were then used as the starting model for the next frequency.

The results of the velocity reconstructions are shown in Figs 8 and 9. The inversion is very effective indeed, given the low-frequency nature of the input data. The results are most dramatic in the upper-crustal regions, where the structure and velocity values have been recovered almost exactly (apart from artefacts at the edges due to insufficient coverage). At mid-crustal depths the velocity values are still nearly correct and the structures are also faithfully recovered. The lower-crustal velocities are recovered with some small errors, and the structure (although not the velocities) of the Moho and the high-velocity mantle material are also recovered, at least in the central region. All of these results are consistent with the expectations derived from the simple examples of the previous section: crustal anomalies are recovered in a tomography-like fashion, whereas Moho structure is recovered in a migration-like fashion. These points can be further verified by an examination of the velocities from the centre of the reconstruction, plotted as graphs on Fig. 9. Here, the slow degradation of the reconstruction with depth is clear. The oscillations on the reconstructions are manifestations of the limited frequency

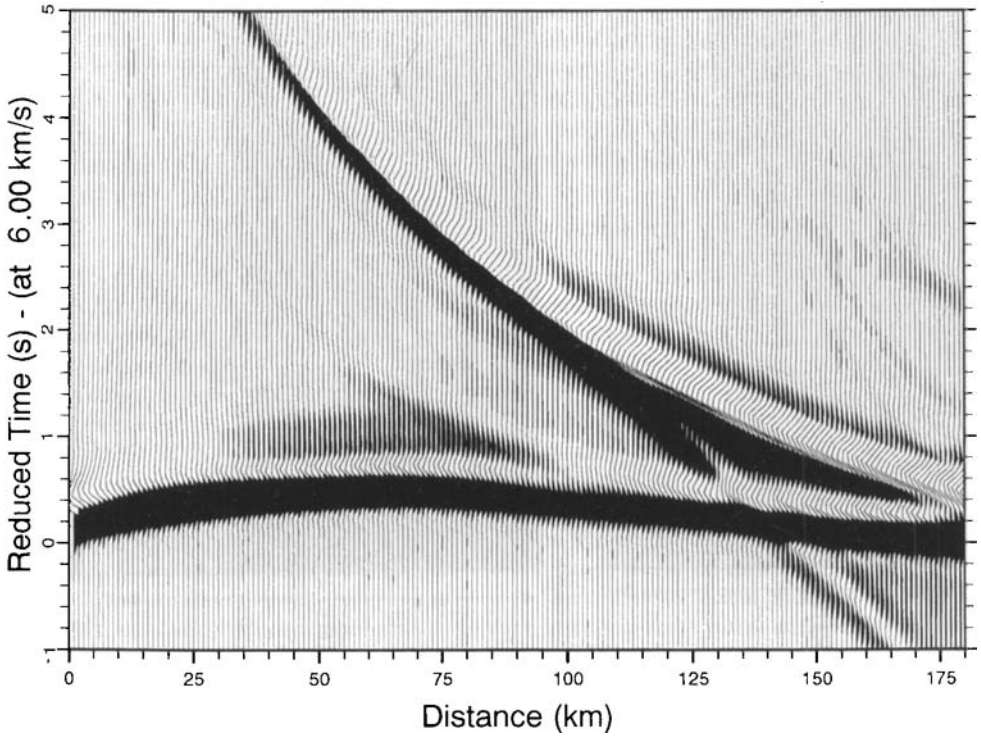

Figure 7. Simulated time-domain data from the generic crustal model (Fig. 6b).

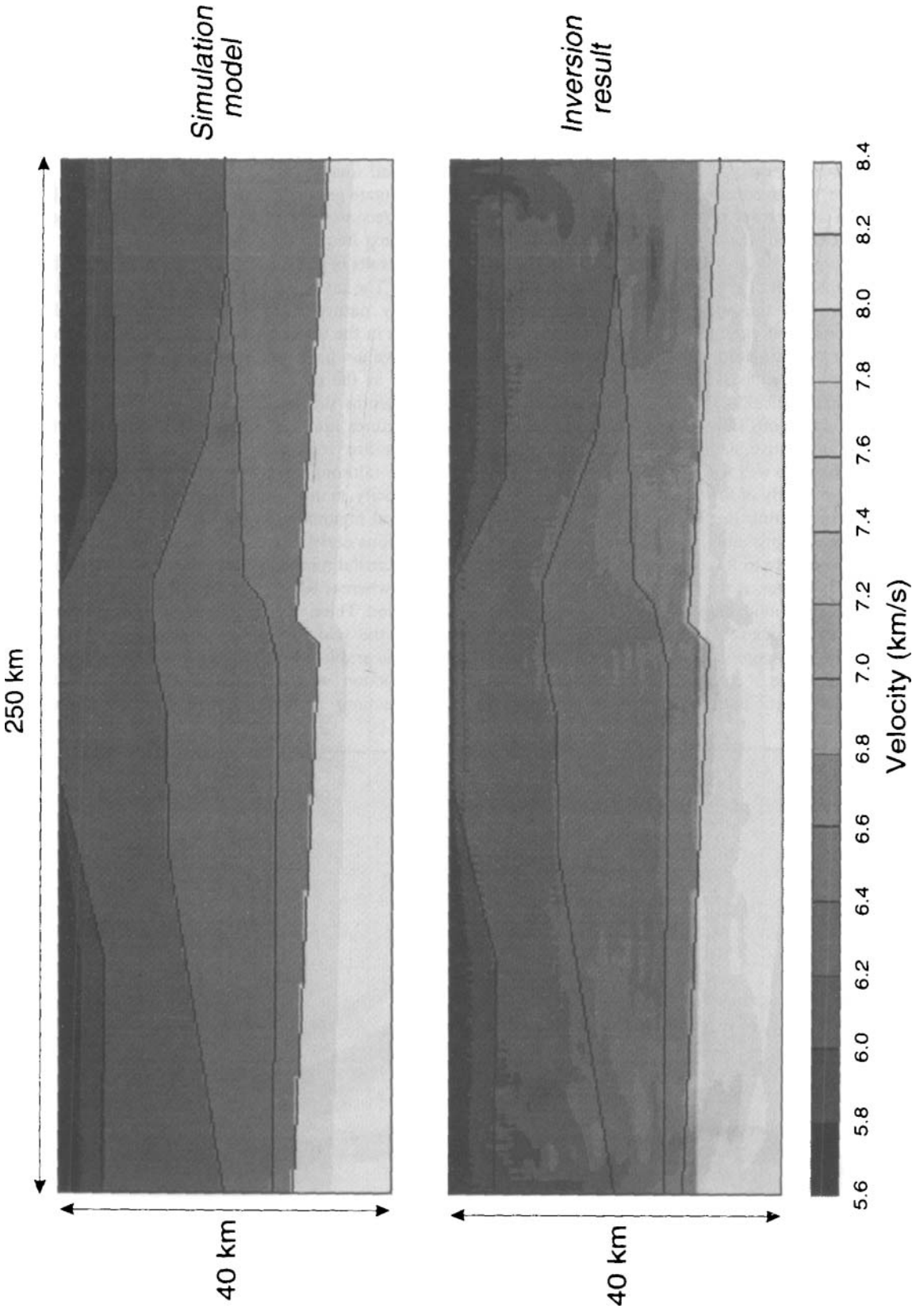

Figure 8. Results (bottom panel) obtained by inverting synthetic data (Fig. 7), compared with the true model (top panel) used to create the data. 12 surface sources, 240 surface receivers and three frequency components (0.5, 1.0 and 2.0 Hz) were used to obtain this result.

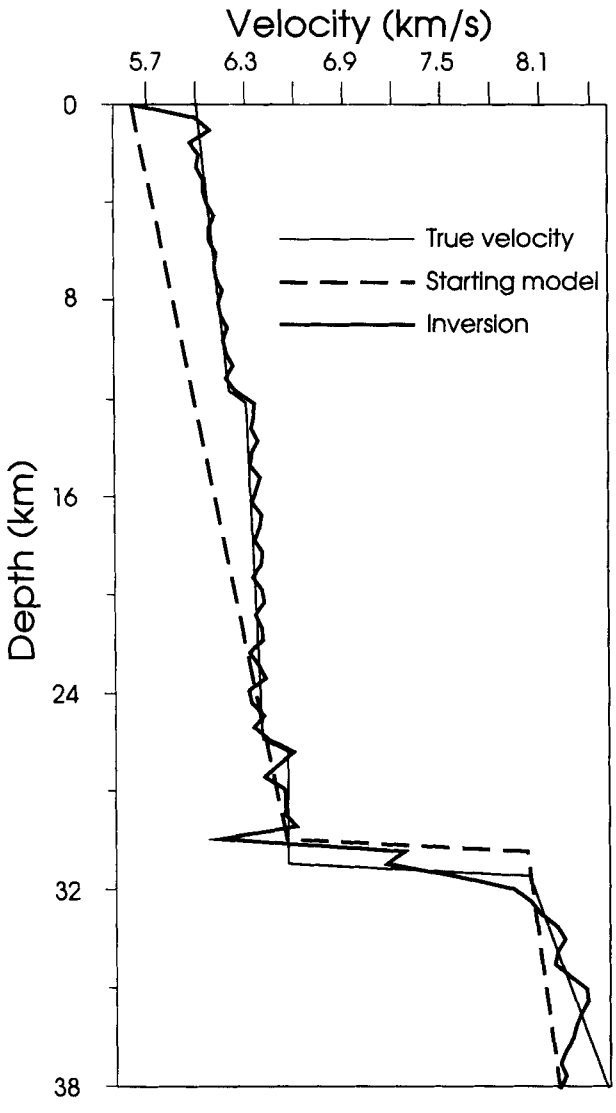

Figure 9. Graphs of seismic velocities from the centre of the simulated survey. The dashed line represents the starting model, the thin line represents the true model and the thick line represents the inversion result (taken from the image in Fig. 8).

content of the input data; these are essentially a Gibbs phenomenon—similar oscillations have been reported for other frequency-domain reconstruction algorithms (e.g. Devaney 1984). The oscillations are not present in the true model, yet the synthetic data for this model match the data for the real model (i.e. the misfit has been reduced almost to zero). Thus these oscillations can be said to be within the 'null space' of the inverse problem. Techniques for controlling null-space artefact in inverse problems are known as regularization (see e.g. Tikhonov & Arsenin 1977). We have used no regularization in solving the inverse problem; we anticipate that some simple form of regularization, such as smoothing, would control the instabilities that lead to these oscillations in our solutions.

It is important to recognize that there are certain difficulties which may be encountered when inverting real data, for which the low-frequency components used here will not exist. In Fig. 10(a) we show the result that is obtained from the same starting model, but here we used only the 2 Hz component of the synthetic data. We have omitted the progression from low frequencies to high frequencies. In this case, the reconstruction fails to converge to the correct answer—a local minimum has been encountered in the objective function due to the limited linear range of the Born approximation used to define the gradient direction in each iteration of the method. This is potentially the most difficult problem that will be encountered in the inversion of real data. To some extent this can be mitigated by using more accurate starting models, such as one derived from traveltime inversion of the picked arrivals. If carried out correctly, such models, while of low resolution, should bring the problem into the zone of influence of the correct global minimum of the objective function. An alternative strategy is to begin the inversion with the near-offset traces only. Since these contain arrivals which have travelled a shorter distance, through shallower geology, the Born approximation will be appropriate, and accurate reconstructions of the shallow layers will be obtained. As the inversion proceeds, the aperture of the input data could be progressively increased by using larger and larger offsets. The effect of this strategy would be to produce velocity models that are progressively more accurate to greater depths. Each time the aperture was increased, the additional data would then be nearly correct and the Born approximation would be adequate to define the new descent direction. Such methods are common in producing velocity models—they are often referred to as 'layer stripping' methods. There are also alternative linearizations, based on the Rytov approximation, that may be appropriate (e.g. Stork 1993). The Rytov approximation requires that individual phases be treated separately, and hence would require a degree of manual intervention.

The image in Fig. 10(b) is the result we obtained using the original strategy (i.e. with all three frequencies), but starting from a model that did not contain the crust–mantle velocity discontinuity. In this case, the crustal velocities are still recovered correctly, and the Moho itself is imaged at the correct depth with the correct structure. However, the magnitude of the velocity discontinuity is not correctly recovered. At this depth, as in the slab model described in the previous section, we recover a band-limited, migrated image of the Moho, rather than a tomographic reconstruction.

CONCLUSIONS

The primary conclusion we draw from this work is that the wavefield inversion of wide-angle crustal data is potentially of great utility. The process is computationally expensive and at the boundary of what is feasible on workstations today, but we expect that the results will show dramatically increased resolution when compared with traveltime inversions. Apart from the additional computational burdens of large-scale, wide-angle crustal data, the difficulties presented by real data will be similar to those encountered with the real crosshole data. We are therefore cautiously optimistic that the method will prove useful on real crustal data.

There is, nevertheless, much to be done to achieve the goal of inverting real crustal data with the methods presented in this paper. Perhaps foremost is the extension of the methods to (visco-)elastic, and possibly anisotropic, wave equations. In principle, this is straightforward, although more expensive in terms of computer resources. As computer hardware continues to develop we anticipate that the necessary resources will

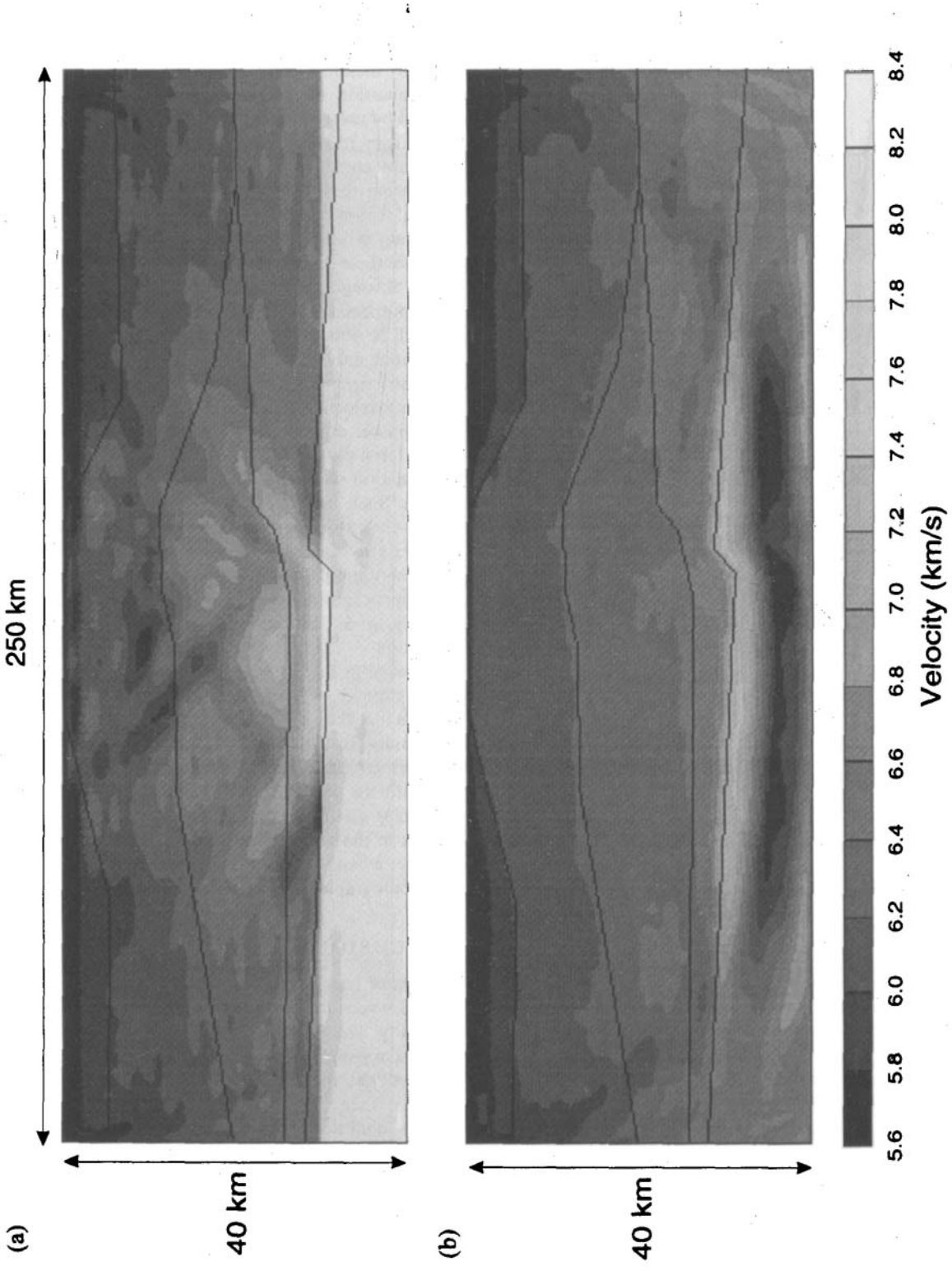

Figure 10. Two images in which an incorrect inversion result was obtained from the simulated crustal data. (a) The image obtained using only a single imaging frequency (2.0 Hz); a local minimum of the objective function is encountered. (b) The image obtained using three frequencies, with no Moho discontinuity in the starting model: a migration-like image of the Moho is obtained.

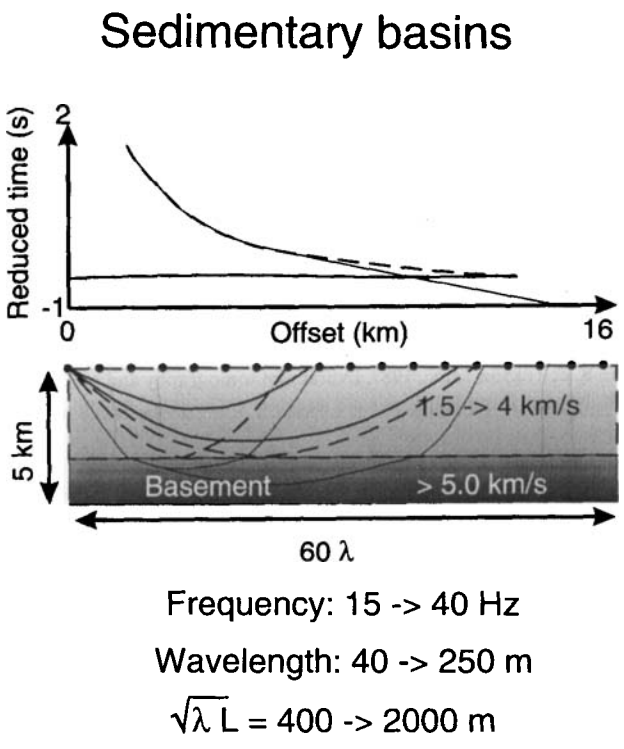

Figure 11. An alternative wide-angle survey that could potentially be inverted using the techniques advocated in this paper.

become commonly available within a few years. In the interim, tests can only be carried out on less widely available platforms, such as large, multi-processor vector machines or massively parallel machines. We also anticipate the need to solve several data-specific problems, such as those related to the limitations of the Born linearization discussed at the end of the previous section.

There are also wider implications that may be drawn from the results of this paper. If we can obtain accurate and well-resolved velocity models from crustal refraction surveys, this would have important implications for exploration seismic surveying. We hope that the inversion of wide-angle crustal surveys will inspire the investigation of sedimentary basins using similar wide-angle survey geometries. Fig. 11 depicts such an application, with approximate rays, frequencies and wavelengths. It is unusual for the imaging of sedimentary basins to be carried out with anything but near-normal incidence reflection data. However, the implications are that we could use the methods proposed in this paper to obtain either more accurate migration velocities, using offsets of the order of 8 km, or velocities of basement rocks, using offsets of up to 16 km. Provided data can be acquired in the range of 10–15 km, refracted arrivals could plausibly be inverted to provide additional constraints on seismic velocities down to reservoir depths. Such results could potentially be used to improve reflection imaging (i.e. migration results), or indeed to delineate sub-basement structures not normally imaged by the reflection method.

REFERENCES

Beydoun, W.B. & Mendes, M., 1989. Elastic ray-Born l_2 migration/inversion, *Geophys. J.*, **97,** 151–160.

Bregman, N.D., Bailey, R.C. & Chapman, C.H., 1989a. Crosshole seismic tomography, *Geophysics,* **54,** 200–215.

Bregman, N.D., Chapman, C.H. & Bailey, R.C., 1989b. Traveltime and amplitude analysis in seismic tomography, *J. geophys. Res.,* **94,** 7577–7587.

Cary, P.W. & Chapman, C.H., 1988. Automatic 1-D waveform inversion of marine seismic refraction data, *Geophys. J.,* **93,** 527–546.

Devaney, A.J., 1984. Geophysical diffraction tomography, *Trans. Inst. Electr. Electron. Eng.,* **GE-22,** 3–13.

Dines, K.A. & Lytle, R.J., 1979. Computerised geophysical tomography, *Proc. Inst. Electr. Electron. Eng.,* **67,** 471–480.

Findlay, M.J., Goulty, N.R. & Kragh, J.E., 1991. The crosshole seismic reflection method in opencast coal exploration, *First Break,* **9,** 509–514.

George, A. & Lui, J.W.H., 1981. *Computer solutions of large positive definite systems,* Prentice-Hall Inc., Englewood Cliffs, NJ.

Hole, J.A., Clowes, R.M. & Ellis, R.M., 1992. Interface inversion using broadside seismic refraction data and three-dimensional travel time calculations, *J. geophys. Res.,* **97,** 3417–3429.

Jo, C.H., Shin, C.S. & Suh, J.H., 1994. Design of an optimal 9 point finite difference frequency-space acoustic wave equation scheme for inversion and modeling, *Geophysics,* accepted.

Lailly, P., 1984. Migration methods: partial but efficient solutions to the seismic inverse problem, in *Inverse problems of acoustic and elastic waves,* eds Santosa, F., Pao, Y.H., Symes, W. & Holland, Ch., Soc. Industr. Appl. Math,

Marfurt, K.J., 1984. Accuracy of finite difference and finite element modeling of the scalar and elastic wave equations, *Geophysics,* **49,** 533–549.

McCarthy, J., Larkin, S.P., Fuis, G.S., Simpson, R.W. & Howard, K.A., 1991. Anatomy of a metamorphic core complex: seismic refraction/wide angle reflection profiling in southeastern California and western Arizona, *J. geophys. Res.,* **96,** 12 259–12 291.

Miller, D.E., Oristaglio, M. & Beylkin, G., 1987. A new slant on seismic imaging: migration and integral geometry, *Geophysics,* **52,** 943–964.

Mora, P.R., 1987a. Nonlinear two-dimensional elastic inversion of multioffset seismic data, *Geophysics,* **52,** 1211–1228.

Mora, P., 1987b. Elastic wavefield inversion for low and high wavenumbers of the *P*- and *S*-wave velocities, a possible solution, in *Deconvolution and inversion: proceedings of a workshop sponsored by the European Association of Exploration Geophysicists et al.,* pp. 321–337, eds Bernabini, M., Carrion, P., Jacovetti, G., Rocca, F. & Treitel, S., Blackwell Scientific Publications, Oxford.

Mora, P., 1988. Elastic wavefield inversion of reflection and transmission data, *Geophysics,* **53,** 750–759.

Polak, E. & Ribiére, G., 1969. Notes sur la convergence de méthodes de directions conjugatées, *Rev. Fr. Inf. Rech. Oper.,* **16-R1,** 35–43.

Pratt, R.G., 1990a. Inverse theory applied to multi-source cross-hole tomography. Part II: elastic wave equation method, *Geophys. Prospect.,* **38,** 311–330.

Pratt, R.G., 1990b. Frequency domain elastic wave modeling by finite differences: a tool for cross-hole seismic imaging, *Geophysics,* **55,** 626–632.

Pratt, R.G. & Chapman, C.H., 1992. Traveltime tomography in anisotropic media–II. Application, *Geophys. J. Int.,* **109,** 20–37.

Pratt, R.G. & Sams, M.A., 1996. Reconciliation of cross-hole seismic velocities with well information in a layered sedimentary environment, *Geophysics,* accepted.

Pratt, R.G., Song, Z.M. & Williamson, P.R., 1994. Can frequency domain inversion of seismic data work?, in *Mathematical Methods in Geophysical Imaging,* pp. 55–65, ed. Zaranttonello, S.E., Proc. SPIE 2033.

Song, Z.-M. & Williamson, P.R., 1995. Frequency-domain acoustic wave modelling and inversion of cross-hole data: Part I—2.5-D modelling method, *Geophysics,* **60,** 784–795.

Song, Z.-M., Williamson, P.R. & Pratt, R.G., 1994. Full wave 2.5D

frequency domain inversion of real crosshole data. *Extended abstracts of the 56th EAEG International Meeting,* Vienna, Austria, paper P063.

Song, Z.-M., Williamson, P.R. & Pratt, R.G., 1995. Frequency-domain acoustic wave modelling and inversion of cross-hole data: Part II—Inversion method, synthetic experiments and real data results, *Geophysics,* **60,** 796–809.

Stork, C., 1993. Hybrid Born and Rytov inversion for seismic applications, in *Mathematical Methods in Geophysical Imaging,* pp. 48–54, ed. Zaranttonello, S.E., Proc. SPIE 2033.

Sun, R. & McMechan, G.A., 1991. Full-wavefield inversion of wide-aperture SH and Love wave data, *Geophys. J. Int.,* **106,** 67–75.

Sun, R. & McMechan, G.A., 1992. 2-D full-wavefield inversion for wide-aperture, elastic, seismic data, *Geophys. J. Int.,* **111,** 1–10.

Tarantola, A., 1984. Inversion of seismic reflection data in the acoustic approximation. *Geophysics,* **49,** 1259–1266.

Tarantola, A., 1987. *Inverse problem theory: Methods for data fitting and parameter estimation,* Elsevier, Amsterdam.

Tikhonov, A. & Arsenin, V., 1977. *Solution of ill-posed problems,* Winston, Washington, D.C.

Williamson, P.R., 1991. A guide to the limits of resolution imposed by scattering in ray tomography, *Geophysics,* **56,** 202–207.

Williamson, P.R., 1993a. Anisotropic crosshole tomography in layered media. Part I: Introduction and methods, *J. Seism. Expl.,* **2,** 107–121.

Williamson, P.R., 1993b. Anisotropic crosshole tomography in layered media. Part II: Applications, results and conclusions, *J. Seism. Expl.,* **2,** 223–238.

Woodward, M.J., 1992. Wave equation tomography, *Geophysics,* **57,** 15–26.

Wu, R. & Toksöz, M.N., 1987. Diffraction tomography and multisource holography applied to seismic imaging, *Geophysics,* **52,** 11–25.